







^{229}Pa cross section measurements via deuteron irradiation of ^{232}Th N. Burahmah ^{1,2,*}, J. R. Griswold ², L. H. Heilbronn ^{1,†}, L. A. Bernstein^{3,4}, A. S. Voyles ³,
J. T. Morrell ³, M. Zach ⁵ and R. Copping²¹*Nuclear Engineering Department, University of Tennessee, Knoxville, Tennessee 37996, USA*²*Radioisotope Science and Technology Division, Oak Ridge National Laboratory, Oak Ridge, Tennessee 37831, USA*³*Department of Nuclear Engineering, University of California, Berkeley, California 94720, USA*⁴*Nuclear Science Division, Lawrence Berkeley National Laboratory, Berkeley, California 94720, USA*⁵*Enrichment Science and Engineering Division, Oak Ridge National Laboratory, Oak Ridge, Tennessee 37831, USA*

(Received 28 April 2023; accepted 31 July 2023; published 23 August 2023; corrected 25 August 2023)

In this work, the previously unmeasured $^{232}\text{Th}(d, 5n)^{229}\text{Pa}$ reaction is reported at deuteron energies of 31.0, 35.2, 41.4, and 49.6 MeV. The irradiation took place at the Lawrence Berkeley National Laboratory 88-Inch Cyclotron. The target processing and analysis were performed at Oak Ridge National Laboratory. The experiment used four thin foils ($\approx 17\text{ mg/cm}^2$) of natural thorium metal in a stacked-target configuration, which were irradiated with a deuteron beam (1 μA) for approximately 11 continuous hours. Column chromatography techniques were implemented to directly assay ^{229}Pa and its low intensity γ -ray emissions. The measured peak of the excitation function of $^{232}\text{Th}(d, 5n)^{229}\text{Pa}$ is $121.9 \pm 12.7\text{ mb}$ at $E_d = 35.2\text{ MeV}$. In addition to ^{229}Pa , the production cross sections of the $^{232}\text{Th}(d, xn)^{234-x}\text{Pa}$ reactions, where $x = 1, 2, 4,$ and 6 , are also reported and compared to previous measurements. The experimental cross sections were compared with calculated cross sections using several reaction modeling codes including PHITS, TALYS, ALICE, COH, and EMPIRE as well as the evaluated nuclear reaction database TENDL.

DOI: [10.1103/PhysRevC.108.024609](https://doi.org/10.1103/PhysRevC.108.024609)**I. INTRODUCTION**

The use of α -emitting radioisotopes to treat cancer and other diseases has recently received renewed attention by the medical field. One technique that has been given considerable attention is targeted alpha therapy (TAT), a procedure used for cancer therapy that capitalizes on the short range and high linear energy transfer (LET) of α particles emitted from isotopes [1–3]. With an LET on the order of 100 keV/ μm , and a range in human tissue of only a few cell diameters, the emitted α particles can produce a lethal dose directed to a tumor cell in human tissue and successfully destroy it without damaging the healthy cells surrounding the tumor. Actinium-225 ($t_{1/2} = 9.920 \pm 0.003\text{ d}$ [4]), and its decay chain product ^{213}Bi ($t_{1/2} = 45.59 \pm 0.06\text{ min}$ [5]) are strong contenders for TAT. Current accelerator-based methods of ^{225}Ac production, which primarily use high-energy protons on ^{232}Th targets, will not meet quantities that are anticipated to be needed worldwide, and coproduce significant quantities of the long-lived radiocontaminant ^{227}Ac ($t_{1/2} = 21.772 \pm 0.003\text{ yr}$ [6]). Researchers are still evaluating the impact of ^{227}Ac presence in accelerator-based irradiation [7–10]. As such, alternative methods of production are being studied, which may offer both improved yields and radiopurity. As an alternative to the challenges of these pathways, production of a high-radiopurity decay precursor allows for the collection of ^{225}Ac ,

free of ^{227}Ac contamination. One such possibility for this approach is the production of ^{229}Pa , which feeds ^{225}Ac through both decay branches ($t_{1/2} = 1.50 \pm 0.05\text{ d}$, 0.48% α to ^{225}Ac , 99.52% ϵ to ^{229}Th [11]). The decay of ^{229}Pa primarily yields ^{229}Th ($t_{1/2} = 7880 \pm 120\text{ yr}$, 100% α [11]), which decays to ^{225}Ra ($t_{1/2} = 14.9 \pm 0.3\text{ d}$, 100% β^- [11]), which in turn decays to ^{225}Ac . As a result, production of high-purity ^{229}Th in large quantities allows for the production of a long-lived “generator,” from which the clinically desirable ^{225}Ac can be “milked” on demand. Thorium-229 is also of interest for use as a quantum clock because of the low energy of its first excited state ($7.6 \pm 0.5\text{ eV}$), which is well within the optical regime [12].

Historically, ^{233}U was the primary source for the production of ^{229}Th , but this production route has been halted until recently. As clinical studies using ^{225}Ac and ^{213}Bi have increased, so has the potential demand for their parent isotope, ^{229}Th . Thus, it has become more important to identify additional production channels, capable of the yields and purity needed to satisfy the demands for generator material.

In this paper, we investigated the excitation functions of (d, xn) reactions on ^{232}Th , as part of an effort to determine ^{229}Th production cross sections. To evaluate its suitability for meeting ^{225}Ac production needs, the $^{232}\text{Th}(d, 5n)^{229}\text{Pa}$ reaction channel will be published here for the first time. Additionally, we present the prediction of reaction cross sections for the interaction of energetic deuterons with a ^{232}Th target resulting in formation of several competing Pa nuclei, including ^{228}Pa , ^{229}Pa , ^{230}Pa , ^{232}Pa , and ^{233}Pa . We used Monte

*Corresponding author: nburahm1@vols.utk.edu†Corresponding author: lheilbro@utk.edu

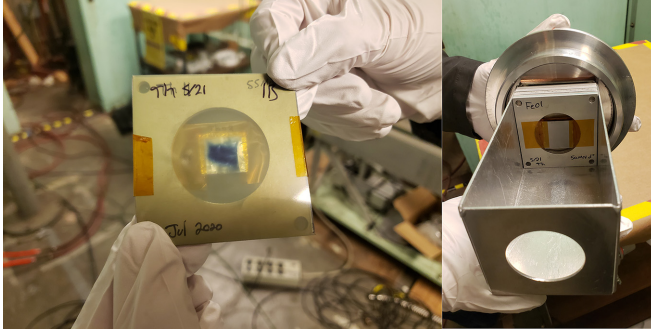


FIG. 1. Photo of a foil secured to aluminum holder (left) and the stacked foils setup (right).

Carlo particle transport code Particle and Heavy Ion Transport code System (PHITS) and the reaction modeling codes ALICE, EMPIRE, COH, and TALYS to calculate the cross sections at incident projectile energies between 5 and 60 MeV. The predicted production cross sections were compared with earlier measured data and predictions when available. Extending our recent work, these comparisons also provide an opportunity to evaluate the predictive capability of modern reaction modeling codes in the mass $A \approx 230$ region.

II. EXPERIMENTAL PROCEDURES

A. Materials and targets

Natural Th foil (0.0125 mm thickness, 99.5% purity) was purchased from Goodfellow Corporation (Coraopolis, PA 15108, USA), and cut into approximately 18 mm \times 18 mm squares. A stack of four such Th foils was constructed, along with 0.025 mm thickness monitor foils of natural Fe (99.5% purity) and natural Cu (99.95% purity), 0.012 mm thickness Al foils (99.99% purity) to encapsulate the Th and prevent loss of target material, and plates of 6061 Al alloy to degrade the beam energy by several MeV between each foil “compartment” (all from Goodfellow Corporation, Coraopolis, PA 15108, USA). A summary of all targets in the stack is presented in Table I.

B. Irradiations

The irradiation was conducted at the 88-Inch Cyclotron at Lawrence Berkeley National Laboratory (LBNL). The 88-Inch Cyclotron is a variable-beam, variable-energy isochronous cyclotron, with maximum energies of 60 MeV and with intensities of up to approximately 15 μ A for deuterons [13]. The experiment took place in Cave 0, a heavily shielded location typically used for experiments that can generate high levels of target activation. The irradiation was performed employing the stacked-target technique as shown in Fig. 1 and analysis methods utilized in our recent work [14–16]. The foils were irradiated with the ≈ 1 μ A of deuteron beam current to ensure that target integrity was not compromised for approximately 10.9 hours, during which the beam current remained stable.

The thin natural iron and copper foils in this stack were placed to measure the deuteron beam current as a function

TABLE I. Specifications of the target stack design in the present work. The deuteron beam enters upstream of foil Fe01 at 50 MeV, and travels through the stack in the order presented here. The 6061 Al degraders have a measured density of approximately 2.68 ± 0.03 g/cm³. Their areal densities were physically measured via their mass (using a Mettler-Toledo analytical balance, 0.01 mg resolution) and their lateral area (using Mitutoyo calipers, 0.01 mm resolution). These listed values were used in all calculations of cross section. An “effective” areal density used only for the consistent determination of deuteron stopping power in the stack was determined using the variance minimization techniques described in this work. Uncertainties listed here are reported at the 1σ level.

Foil	Target thickness (mg cm ⁻²)	Average energy (MeV)
Fe01	20.05 ± 0.05	49.85 ± 0.47
Al wrapper 01F	1.54 ± 0.02	49.70 ± 0.45
Th01	17.15 ± 0.08	49.61 ± 0.46
Al wrapper 01B	1.54 ± 0.02	49.52 ± 0.45
Cu01	22.25 ± 0.1	49.35 ± 0.47
Al degrader B-1	415 ± 5	45.62 ± 2.32
Fe02	20.11 ± 0.06	41.73 ± 0.53
Al wrapper 02F	1.53 ± 0.02	41.55 ± 0.52
Th02	17.17 ± 0.08	41.45 ± 0.52
Al wrapper 02B	1.53 ± 0.02	41.34 ± 0.52
Cu02	22.05 ± 0.09	41.16 ± 0.54
Al degrader C-1	262 ± 3	38.39 ± 1.73
Fe03	19.98 ± 0.10	35.53 ± 0.61
Al wrapper 03F	1.55 ± 0.03	35.33 ± 0.59
Th03	17.37 ± 0.17	35.21 ± 0.60
Al wrapper 03B	1.55 ± 0.03	35.10 ± 0.59
Cu03	22.24 ± 0.07	34.88 ± 0.62
Al degrader E-1	68.3 ± 0.8	33.93 ± 0.81
Al degrader E-2	68.3 ± 0.8	32.39 ± 0.84
Fe04	20.29 ± 0.059	31.39 ± 0.67
Al wrapper 04F	1.55 ± 0.02	31.17 ± 0.65
Th04	17.51 ± 0.25	31.04 ± 0.66
Al wrapper 04B	1.55 ± 0.02	30.91 ± 0.65
Cu04	22.21 ± 0.07	30.68 ± 0.68

of position in the stack, using the International Atomic Energy Agency (IAEA)-recommended $^{nat}\text{Fe}(d, x)^{56}\text{Co}$ and $^{nat}\text{Cu}(d, x)^{65}\text{Zn}$ monitor reactions [17]. The propagated uncertainty in deuteron fluence is calculated as the quadrature sum of (1) the uncertainty in quantified end-of-bombardment activity, (2) uncertainty in the duration of irradiation (conservatively estimated at 100 s, to account for any transient changes in beam current), (3) uncertainty in foil areal density, (4) uncertainty in monitor product half-life (included, but normally negligible), (5) uncertainty in IAEA-recommended cross section [17], and (6) uncertainty in differential deuteron fluence (from transport simulations).

Determination of the deuteron beam energy distribution in each element of the target stack was performed using the Andersen-Ziegler stopping power formalism, as implemented in the Curie Python package [18]. This transport calculation was used to determine the differential deuteron fluence and flux-weighted average deuteron energy for each foil in the stack, and the full width at half maximum of the deuteron

energy spectrum was used to report the energy uncertainty for each foil. Similarly to previous work [14–16], the “variance minimization” technique was used to obtain the correct deuteron energy spectrum for each foil and reduce uncertainty in beam fluence through an iterative correction of stopping power in transport calculations. Notably, this measurement serves as the first extension of this technique to a stack irradiation using a deuteron beam. However, the same core assumption still stands: inaccurate calculation of the deuteron beam stopping power can be corrected by varying the density of the targets until the activities from the Fe and Cu monitor reactions are consistent throughout the stack.

In this work, the global stopping power in transport calculations was uniformly scaled for all materials in the stack in an iterative fashion (in steps of 0.001%) within the range of $\pm 15\%$ from nominal values to find the iteration that led to a clear minimum in variance between monitor reactions in the rearmost stack position (Fe04/Cu04). In our previous measurements, multiple monitor reactions in the same foil were used to confirm the beam energy and current in each foil [16,19]. However, in the present work, the $^{nat}\text{Cu}(d,x)^{62,63}\text{Zn}$ monitor reactions could not be employed because of the amount of fluence used in this stack. By the time the monitor foils had decayed to activities capable of being counted on the high-purity germanium (HPGe) detector, the short-lived $^{62,63}\text{Zn}$ monitor products had completely decayed out. This is exacerbated by the relative paucity of deuteron monitor reactions in the IAEA evaluation, relative to the proton monitor standards. As a result, the variance minimization process leads to a broad minimum in the reduced χ^2 for the Fe04/Cu04 monitor reactions, converging on a deuteron stopping power scalar correction factor of 0.98749 from nominal values needed to achieve best agreement with the IAEA monitor standards. The magnitude of this correction (an approximately 1.25% reduction in deuteron stopping power) is very modest, and well within the range seen in our previous work [14–16]. This is commonly seen for cases where few monitor reactions exist or cases in which all available monitor reactions are monotonic in energy. Monitor reaction excitation functions that include some products that rise in an energy window where others are falling or reactions that have energetic thresholds midway through a target stack, yield great sensitivity during variance minimization, helping determine the correct energy distributions in each foil. Although they were not used to measure beam current, experimental data for the $^{nat}\text{Cu}(d,x)^{58,60}\text{Co}$ [20,21] and $^{nat}\text{Fe}(d,x)^{54}\text{Mn}$ [22–28] reactions were used to validate the beam currents determined via the IAEA monitor reactions $^{nat}\text{Fe}(d,x)^{56}\text{Co}$ and $^{nat}\text{Cu}(d,x)^{65}\text{Zn}$. These reactions were chosen because of the lifetimes of the reaction products, as well as because they are both strongly fed and have products that are not populated via decay feeding or any other competing reaction channels. As in previous work [16], the correlated uncertainty-weighted average beam current was calculated for each stack compartment based on the $^{nat}\text{Fe}(d,x)^{56}\text{Co}$ and $^{nat}\text{Cu}(d,x)^{65}\text{Zn}$ monitor reactions. This average beam current (and its propagated uncertainty) could be used to calculate the “apparent” values of the IAEA cross sections for each monitor reaction. The additional constraints added by these experimental data

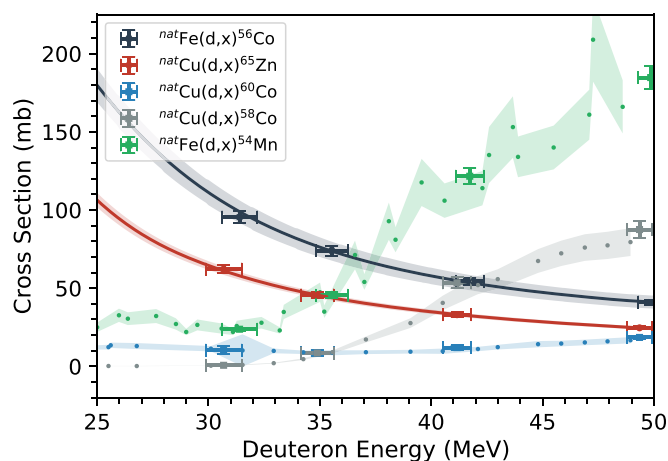


FIG. 2. Plot of the apparent cross sections for the IAEA-recommended $^{nat}\text{Fe}(d,x)^{56}\text{Co}$ and $^{nat}\text{Cu}(d,x)^{65}\text{Zn}$ monitor reactions [17] in each of the Cu and Fe monitor foils. The effects of the variance minimization technique show a minor improvement in reduced χ^2 when comparing the results before and after this process. This shows the agreement of variance minimization converging on a stopping power correction factor of approximately 0.9875 from nominal values (i.e., a 1.25% reduction in deuteron stopping power for all materials), validated by agreement to both the IAEA evaluation and experimental data for the $^{nat}\text{Cu}(d,x)^{58,60}\text{Co}$ [20,21] and $^{nat}\text{Fe}(d,x)^{54}\text{Mn}$ [22–28] reactions.

channels provide a visual validation and show that the convergence of variance minimization predicts a transport solution that is consistent with both IAEA and experimental data. The results of this process are shown in Fig. 2.

C. Chemical separations

After irradiation, the foils were shipped to Oak Ridge National Laboratory for chemical separation and analysis. Since one of the main objectives of this work was to assay ²²⁹Pa through its low intensity γ -ray emissions (119.0 keV, $0.129 \pm 0.007\%$ [11]), the targets were dissolved, and Pa product nuclei were separated from fission products and coproduced actinides via ion exchange chromatography.

Before dissolution, the foils were assayed via γ -ray spectroscopy to establish a pre-separation activity, as described in Sec. IID. Then, each foil was dissolved in 10 mL of 10 M optima-grade hydrochloric acid (HCl) and a few drops of 2 M hydrogen fluoride. BioRad gravity-flow disposable polypropylene (PP) columns with 0.5–1 mL of MP1 Cl⁻ anion exchange resin with resin size of 100–200 mesh were used for the chemical isolation of Pa. Figure 3 shows a graphical representation of the chemical separation. This separation methodology was developed as part of the research and development for the DOE Tri-Lab ²²⁵Ac production effort [29–31]. The short half-life of ²²⁹Pa ($t_{1/2} = 1.50 \pm 0.05$ d [11]) necessitated that the chemical separation be completed quickly and efficiently over a 4-day period.

To determine the efficiency of the overall chemical separation, the coproduced ²³²Pa (1.31 ± 0.02 d [32]) was used as a radiotracer. Protactinium-232 has similar half-life to ²²⁹Pa

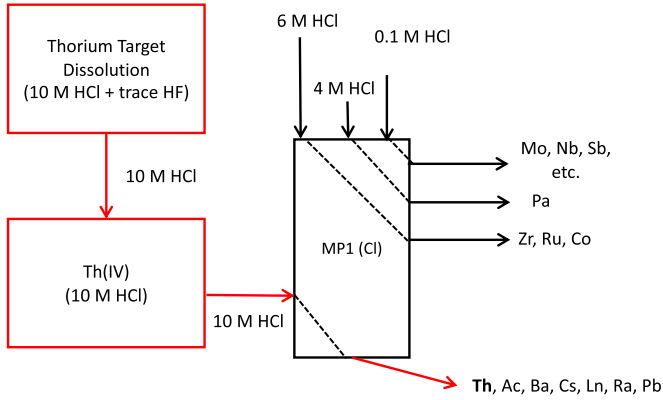


FIG. 3. Ion-exchange chromatography flowchart.

and emits a γ ray at 894.351 keV ($19.6 \pm 0.3\%$ [32]) that has no interferences from γ rays emitted by trace isotopes still present in the Pa fraction after chemical separation such as ^{95}Nb , ^{99}Mo , and ^{115g}Cd . The Pa was collected in six fractions of 4 M HCl (0.5–2 mL per fraction) to increase the number of fractions that would be free of radiopurities. The chemical separation efficiencies range from 6% to 26%. Some of the radiopurities such as ^{95}Zr , ^{103}Ru , and ^{57}Co were eluted from the column before the Pa fraction in 6 M HCl. Other radiopurities such as ^{99}Mo , ^{95}Nb , and ^{125}Sb were eluted from the column after the Pa fraction in 0.1 M HCl.

D. Radioactivity measurements

The γ -ray spectroscopy measurements were conducted using a well-shielded CANBERRA GEM series (model no. GEM20-70 and serial no. 50-P22797B) HPGe coaxial detector coupled to CANBERRA GENIE 2000 software for spectrum acquisition. The detector has a relative efficiency of 20% and a resolution of 0.74 keV at 122 keV and 2.0 keV at 1332 keV. The detector calibration was performed using a ^{166m}Ho source. Counting times varied from 5 minutes to 36 hours, and the calibration source was counted between 2 and 60 cm from the detector, depending on the spectrum activity. Table II summarizes the nuclear decay data of radioisotopes relevant to this work. Equation (1) was used to calculate the experimental cross section, where A_0 is the activity at the end of bombardment, N is the areal density of the target (atoms cm^{-2}), φ is beam current (deuteron s^{-1}), $\varepsilon_{\text{chem}}$ is the overall chemical separation efficiency, λ is the decay constant, and t is the irradiation time. Cross section

propagated uncertainty is calculated from the quadrature sum of the uncertainty in the radionuclide activity A_0 (i.e., counting statistics, γ -ray intensity, etc., $\approx 1\%$ – 6%), the uncertainty in beam current ($\approx 4\%$), the uncertainty in the chemical separation efficiency ($\approx 2\%$ – 5%), the uncertainty in detector efficiency ($\approx 5\%$), and uncertainty in target areal density ($\approx <2\%$).

$$\sigma = \frac{A_0}{N\varphi\varepsilon_{\text{chem}}(1 - e^{-\lambda t})}. \quad (1)$$

III. COMPUTATIONAL METHODS

Because experimental data for $^{232}\text{Th}(d, x)$ are extremely sparse, a suite of modern reaction modeling codes have been used to estimate reaction cross sections. These may be used to interpolate between experimental data to calculate thick-target yields. Owing to the scarcity of (d, x) reaction data in this mass region, this measurement offers an opportunity to benchmark these reaction codes against experimental data and potentially gain insight into how the predictive power of these codes may be improved by identifying where their models fail to reproduce measurements. A brief overview of each code is provided here, and additional details can be found in a recent review [36]. Although each code can be tuned to reproduce our experimental data, we have explicitly chosen to run all codes using their default parameters. Parameters may be arbitrarily chosen to fit a particular reaction channel, but our work has shown that such a channel-by-channel optimization leads to false minima solutions that lack global accuracy and can mislead any physics interpretation of modeling [15,37]. All major exit channels must be observed and tuned simultaneously to obtain model parameters that avoid local minima in χ^2 . However, because only (d, xn) products and not the large (d, f) channel were observed, we present only default modeling calculations to assess their relative “out of the box” performance.

A. PHITS calculations

PHITS [38] is a Monte Carlo particle transport simulation code developed by the Japan Atomic Energy Agency. PHITS transports all particles over a wide range of energies, and users have the option to select the physics models to be used. Facility shielding design, medical physics, radiation protection, geoscience, and isotope production are some of the applications of the code.

TABLE II. Nuclear decay data of radioisotopes measured in this work. These data have been used for all calculations of measured cross sections and were taken from the most recent Nuclear Data Sheets evaluation for each mass chain [11,32–35].

Isotopes	Half-life	E_γ (keV)	I_γ (%)	$^{232}\text{Th}(d, xn)$ reaction threshold (MeV)
^{228}Pa	22 ± 1 h	911.204	23.0 ± 1.1	29.02
^{229}Pa	1.50 ± 0.05 d	119.0	0.129 ± 0.007	21.86
^{230}Pa	17.4 ± 0.5 d	951.88	29.6 ± 1.8	16.01
^{232}Pa	1.31 ± 0.02 d	894.351	19.6 ± 0.3	3.54
^{233}Pa	26.975 ± 0.013 d	311.901	38.2 ± 0.4	0

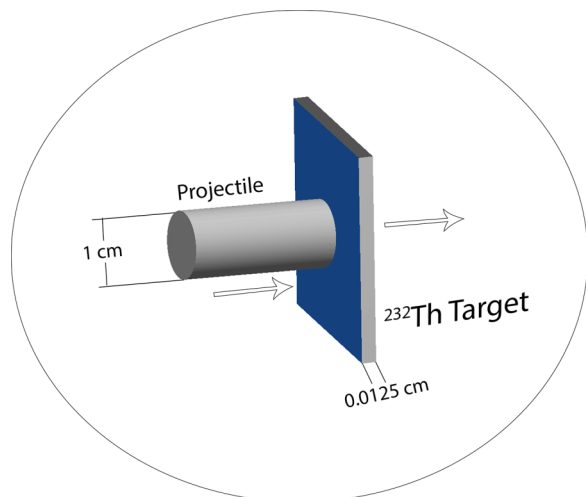


FIG. 4. The geometry of target and projectiles used in the PHITS calculations (not to scale).

In this work, we used PHITS version 3.1 with the intranuclear cascade (INCL4.6) and evaporation (GEM) models to calculate the reaction cross sections for the interaction of deuteron particles incident upon a ^{232}Th target [39]. For the total cross section, the KUROKAMA model was employed [40]. Unlike the other codes used in this work, PHITS couples particle transport to reaction modeling, and thus requires a spatial model of the target stack for calculations. Figure 4 graphically illustrates the simple geometry used in the PHITS calculations: a rectangular solid representing a ^{232}Th foil target with a thickness of 0.0125 cm. The projectile was a cylindrical source with a uniform distribution throughout a 0.5 cm radius. The PHITS *T-Yield* tally was used to track the production of nuclides through all reactions. In each of these simulations, 5×10^8 incident particles were used, and the energy of the projectiles ranged from 5 to 70 MeV. Further details about the simulation process and cross section calculation can be found in this publication [41].

B. TALYS calculations and the TENDL library

TALYS is a nuclear reaction modeling code used in a variety of application areas [42,43] that uses Hauser-Feshbach statistical and exciton pre-equilibrium reaction models. It supports the modeling of incident neutrons, light ions (up to α particles), and photons, up to 200 MeV. In this work, we used version TALYS-1.95. The default nuclear models used in TALYS are the Koning-Delaroche optical model parametrization for both protons and neutrons [44], a TALYS-specific folded potential for the optical model for both α particles and deuterons [43,45,46], a Brink-Axel Lorentzian model for the $E1$ γ -strength function [43], and the Gilbert-Cameron nuclear level density model [47].

TENDL is a nuclear data library generated through the use of TALYS and a number of companion codes. This process uses experimental data, where available, to optimize reaction modeling parameters in TALYS calculations on a nuclide-by-nuclide and local channel basis, resulting in an evaluated library [48]. It also provides evaluated results for secondary

particle production spectra, angular distributions, and production yields for thick targets, which is useful for isotope production applications. As the data in TENDL have been tuned to measurements, it is commonly the first choice for experimenters in need of estimated production cross sections for initial designs of isotope production targets, as it generally offers superior predictive capacity over default TALYS calculations. For this reason, TENDL was chosen as the back-end source of cross section data for the IAEA’s Medical Isotope Browser for target yield calculations, powered by the ISOTOPIA tool [49]. In this work, we used data from the TENDL-2021 database.

C. ALICE calculations

ALICE is a Monte Carlo code using the Weisskopf–Ewing evaporation and geometry-dependent hybrid precompound decay models, which accepts incident photons, protons, neutrons, and heavy ions [50,51]. The Weisskopf-Ewing formalism is another simpler statistical model for compound nuclear reactions, but, unlike the Hauser-Feshbach formalism, it does not account for conservation of angular momentum and parity. However, when used at the high energies relevant to isotope production, the quantum effects become somewhat diluted and weaker, which is due to the larger number of degrees of freedom at these excitation energies. In this work, we used version ALICE-2020. The default nuclear models used in ALICE are the Nadasen optical model parametrization for both protons and neutrons [52], a parabolic diffuse-well potential for the optical model for both α particles and deuterons [53], a Berman-Fultz Lorentzian model for the $E1$ γ -strength function [54], and the Kataria-Ramamurthy-Kapoor nuclear level density model [55,56].

D. EMPIRE calculations

EMPIRE is another Hauser-Feshbach statistical model code, which accepts up to 150 MeV incident particles including neutrons, protons, light ions (up to α particles), and limited support for heavy ions [57]. While it is primarily designed and optimized for modeling and evaluation of (n, x) reactions, it is still a useful tool for estimating excitation functions and associate reaction observables for light ion-induced reactions up to intermediate isotope production energies. In this work, we used version EMPIRE-3.2.3. The default nuclear models used in EMPIRE are the Koning-Delaroche optical model parametrization for both protons and neutrons [44], the An optical model parametrization for deuterons [58], the Avrigeanu (2009) optical model parametrization for α particles [59], a modified Lorentzian model for the $E1$ γ -strength function [60], and the enhanced generalized superfluid nuclear level density model [61].

E. COH calculations

COH is a hybrid coupled-channel and Hauser-Feshbach statistical code, designed for neutrons and light ions above 1 keV on targets of $A > 20$ [62–65]. This code provides complete information on nuclear reactions, including reaction cross sections as well as energy and angular distributions

TABLE III. Effective production cross sections (in mb) of selected radionuclides at 31–50 MeV deuteron energy. Uncertainties listed here are reported at the 1σ level. (σ_c is the cumulative cross section and σ_i is the independent cross section.)

Energy (MeV)	^{233}Pa (σ_c)	^{232}Pa (σ_i)	^{230}Pa (σ_i)	^{229}Pa (σ_i)	^{228}Pa (σ_i)
31.0	75.0 ± 5.2	40.6 ± 2.7	161 ± 15	89.3 ± 8.5	
35.2	56.1 ± 4.0	31.3 ± 2.1	71.9 ± 6.6	122 ± 11	2.31 ± 0.21
41.4	33.1 ± 2.3	21.9 ± 1.4	58.0 ± 5.4	43.7 ± 4.5	34.9 ± 3.0
49.6	30.5 ± 2.6	20.4 ± 1.4	47.3 ± 4.9	38.2 ± 4.8	31.6 ± 3.1

of secondary particles. Although it is tuned primarily for neutrons below $E_n = 14$ MeV, our recent work shows that it generally performs well for (p, x) reactions at energies below 200 MeV. This work presents the first time our group has benchmarked its performance for (d, x) reactions against other reaction modeling codes. In this work, we used version COH-3.5.4 (“Miranda”). The default nuclear models used in COH are the Koning-Delaroche optical model parametrization for both protons and neutrons [44], the An optical model parametrization for deuterons [58], the Avrigeanu (1994) optical model parametrization for α particles [66], a generalized Lorentzian model for the $E1$ γ -strength function [62], and the Gilbert-Cameron nuclear level density model [47].

IV. RESULTS

The experimentally measured cross sections for the Pa radionuclides produced in this work are available in Table III.

In this work, Fig. 5 illustrates the cumulative production cross sections of ^{233}Pa , whereas Figs. 6–9 show the independent production cross sections of $^{232,230,229,228}\text{Pa}$. The results are compared to experimental cross sections previously reported in the literature, when available, and to the estimates from the suite of reaction modeling codes discussed in Sec. III. Notably, as discussed earlier, all calculations from these codes have been performed using default parameter values, to assess their predictive power.

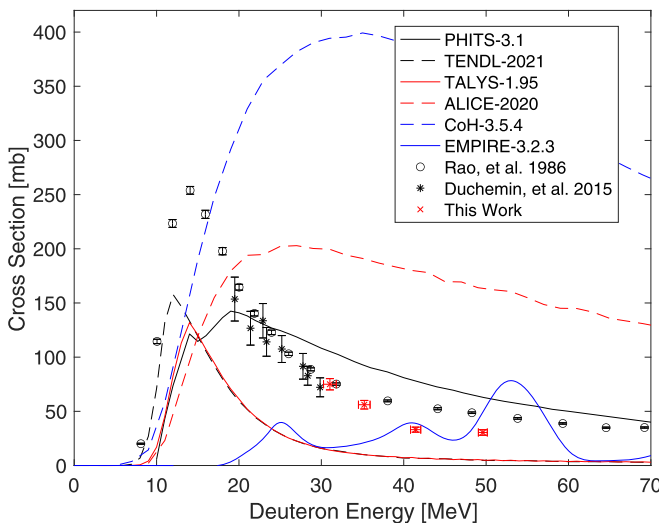


FIG. 5. Comparison of the $^{232}\text{Th}(d, n)^{233}\text{Pa}$ cumulative calculated cross section with experimental data.

Note, the calculated cross sections from all modeling codes are time independent and do not include contributions from the decay of any precursors, nor do they include the decay of the product nuclei itself. The yield of particular product nuclei can occur through both direct and indirect (e.g., decay of short-lived precursors) reaction channels. In cases where data were available, we compared the simulation results with experimental data that include feeding of the product nuclei in question from the decay of short-lived precursors. For example, the experimentally measured ^{233}Pa cross sections also include the contributions from the indirect decay route from ^{233}Th . In such cases, for a direct comparison to experimental data, we plot the calculated cross sections including contributions from the indirect route (e.g., from ^{233}Th decay) assuming that $>99\%$ of the precursors have decayed into ^{233}Pa . In those cases, the cross sections are referred to as “cumulative” cross sections rather than “independent” cross sections.

A. $^{232}\text{Th}(d, n)^{233}\text{Pa}$ production cross sections

The measured cross sections for ^{233}Pa are presented in Fig. 5. In Fig. 5, our measured cross sections were cumulative and included the contribution of $^{232}\text{Th}(d, p)^{233}\text{Th}$. ^{233}Th ($t_{1/2} = 21.83 \pm 0.04$ min [35]) decays via β^- emission (β^- , 100%) to ^{233}Pa . Since the target chemical separation took place approximately 24 hours after irradiation (because of shipping times), it is assumed that all ^{233}Th decayed into ^{233}Pa before assay. Our maximum cross section value for

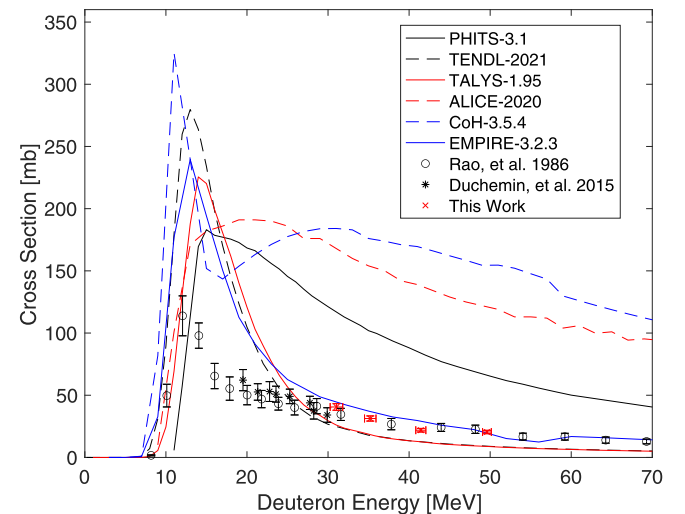


FIG. 6. Comparison of the $^{232}\text{Th}(d, 2n)^{232}\text{Pa}$ calculated independent cross section with experimental data.

$^{232}\text{Th}(d, n)^{233}\text{Pa}$ is 75.0 ± 6.4 mb, and it occurs at approximately $E_d = 31.0$ MeV. The calculated cross sections were within a factor of 2–5 with the measured cross sections. None of the codes do a particularly good job of reproducing this reaction channel. TALYS and TENDL both appear to predict the correct shape for the channel, but they underestimate its magnitude by approximately 40%, reaching the compound peak approximately 4 MeV too low. COH and ALICE both significantly overestimate the entire channel magnitude and fail to predict the shape. Indeed, no compound peak is observed, but rather a slow rise to a broad and slowly tailing continuum. This behavior suggests issues in these codes with calculation of transmission coefficients for the (d, xn) channels and likely with the spin distribution of the excited compound nuclear system. The fact that we see no clear compound peak for a (d, n) channel suggests that preequilibrium is being significantly overestimated compared to the compound mechanism component and that the excitation energy from the incoming deuteron dissipates too quickly as it spreads over the compound system. As this behavior is strongly spin dependent, it is not surprising to see this behavior in ALICE and COH because ALICE does not conserve angular momentum in its calculations, and the Kalbach pickup parametrization implemented in COH for incident deuterons is known to overestimate the preequilibrium mechanism component. PHITS predicts a small magnitude compound peak near 14 MeV, underestimating the peak like TALYS and TENDL, but they also predict the broad pre-equilibrium component seen in COH and ALICE, albeit at a far lower magnitude. It is possible that this double-peaked shape is the feeding contribution from the short-lived ^{233}Th produced via (d, p) , but as this channel is reported as a cumulative cross section, it is impossible to separate these two components. Owing to the highlight of the Coulomb barrier in Pa, the (d, p) contribution should be very weakly fed relative to (d, n) .

The effective cross sections were compared with cross sections from the literature for the same reaction [67,68]. The measurements agree reasonably well with the data reported from Duchemin *et al.* [67] and Rao *et al.* [68] up to approximately 35 MeV, but we report lower cross sections above this energy by approximately 60%, suggesting a weaker preequilibrium component than previously reported. Note, that the experiment conducted by Rao *et al.* occurred in 1986 and used different γ -ray intensity values than reported in the Nuclear Data Sheets [11,32–35]. For ^{233}Pa γ -ray intensity at 311.901 keV, Rao *et al.* used 37%, but the intensity reported in the Nuclear Data Sheets is $38.2 \pm 0.4\%$, meaning that our intensity is higher by $\approx 3\%$ [35]. In addition, Rao *et al.* used energy loss values for U. Thorium values were not available in [69], so the energy estimation for the cross section is shifted. Also, there is no mention of the methodology or uncertainty of the beam current. These could explain the discrepancies of the cross section above 35 MeV.

B. $^{232}\text{Th}(d, 2n)^{232}\text{Pa}$ production cross sections

The independent measured and calculated cross sections for the $^{232}\text{Th}(d, 2n)^{232}\text{Pa}$ reaction are shown in Fig. 6. Protactinium-232 ($t_{1/2} = 1.31 \pm 0.02$ d [32]) decays via

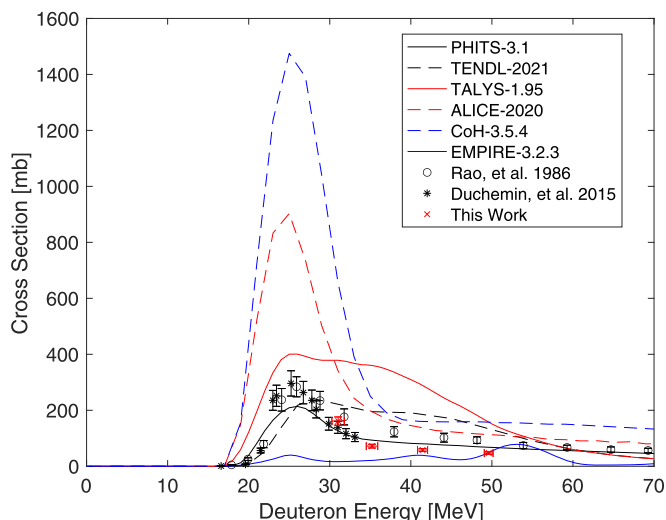


FIG. 7. Calculated and measured independent cross sections for $^{232}\text{Th}(d, 4n)^{230}\text{Pa}$ reaction.

β^- emission (β^- , 100%) to ^{232}U . As noted previously, ^{232}Pa was used as a radiotracer for the chemical separation. Figure 6 compares our experimentally measured independent cross sections with the calculated cross sections. The maximum value of our excitation function for $^{232}\text{Th}(d, 2n)^{232}\text{Pa}$ is 40.6 ± 3.3 mb, and it occurs at approximately $E_d = 31.0$ MeV. Above 25 MeV, our data were in excellent agreement with TALYS, TENDL, and EMPIRE. These codes all correctly predict the shape of this channel, but they consistently overestimate the magnitude of this channel’s compound peak by a factor of approximately 2–3. COH does correctly predict the presence of the compound peak, but it misses the peak energy by approximately 3 MeV, and, along with ALICE and PHITS, it incorrectly predicts the channel shape by suggesting a broad second peak transitioning into preequilibrium at higher energies. The experimental cross sections were compared with previously reported cross sections [67,68] in Fig. 6. Cross sections from this work agree well with previously reported data from Duchemin *et al.* [67] and Rao *et al.* [68].

C. $^{232}\text{Th}(d, 4n)^{230}\text{Pa}$ production cross sections

Figure 7 shows our independent experimental and calculated cross sections for ^{230}Pa production. Protactinium-230 ($t_{1/2} = 17.4 \pm 0.5$ d [33]) decays via electron capture (EC, 92.2%) to ^{230}Th and via β^- emission (β^- , 7.8%) to ^{230}U ($t_{1/2} = 20.8 \pm 2.1$ d [70]). Uranium-230 is another promising candidate for TAT for cancer, as a generator for ^{226}Th ($t_{1/2} = 30.57 \pm 0.10$ min, 100% α [71]), which rapidly undergoes a series of decays releasing an additional four α particles, leading to a high combined dose to targeted cancer cells [72–74]. The excitation function of the $^{232}\text{Th}(d, 4n)^{230}\text{Pa}$ reaction is shown in Fig. 7. As presented, our maximum independent cross section of ^{230}Pa at 161 ± 17 mb occurs at approximately $E_d = 31.0$ MeV. The data are within a factor of 2 of the PHITS calculated data. Notably, all codes seem to do a good job of predicting the shape of this channel except TENDL,

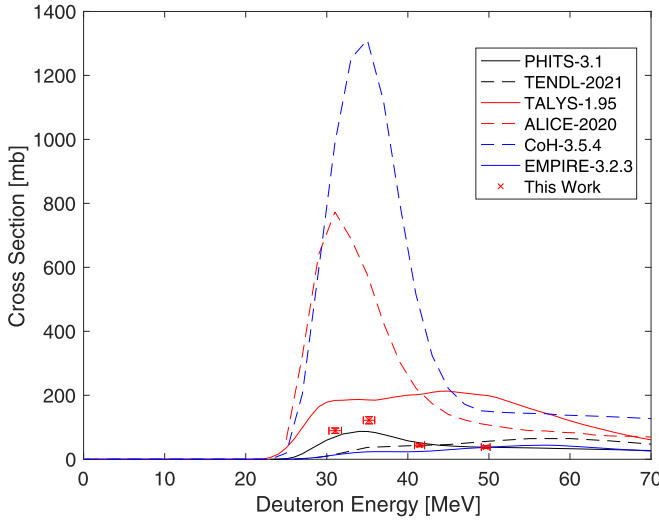


FIG. 8. Comparison of $^{232}\text{Th}(d, 5n)^{229}\text{Pa}$ independent calculated cross section with experimental data.

though TALYS predicts far stronger preequilibrium feeding than is observed in the experimental data. All other codes significantly overestimate the cross sections, but the predictions from EMPIRE underestimate the channel and predict additional “bumps” in the excitation function near $E_d = 42$ and 55 MeV. Our experimental cross sections for the $^{232}\text{Th}(d, 4n)^{230}\text{Pa}$ reaction channel are compared with reported literature values [67,68] in Fig. 7 and are in excellent agreement. For ^{230}Pa γ -ray intensity at 951.88 keV, Rao *et al.* used 28%, but the intensity reported in the Nuclear Data Sheets is $29.6 \pm 1.8\%$, meaning our intensity is higher by $\approx 5\%$ [33].

D. $^{232}\text{Th}(d, 5n)^{229}\text{Pa}$ production cross sections

Protactinium-229 ($t_{1/2} = 1.50 \pm 0.05$ d [11]) decays via electron capture (EC, 99.5%) to ^{229}Th ($t_{1/2} = 7880 \pm 120$ yr [11]) and via α emission (α , 0.5%) to ^{225}Ac ($t_{1/2} = 9.920 \pm 0.003$ d [4]). In this work, the production of ^{229}Pa from bombardment of ^{232}Th by deuterons below 50 MeV is the primary interest because of its decay channels that lead to the production of ^{225}Ac . The measured independent cross sections for the $^{232}\text{Th}(d, 5n)^{229}\text{Pa}$ reaction are reported here for the first time.

Figure 8 shows the experimental and calculated independent cross sections for the $^{232}\text{Th}(d, 5n)^{229}\text{Pa}$ reaction. The peak of our observed excitation function is 122 ± 13 mb and occurs at approximately $E_d = 35.2$ MeV. Despite the lack of any prior experimental data, all of the modeling codes do a good job of predicting the shape of this reaction channel, though TENDL fails to predict the shape of the channel. Above 40 MeV, the data were in excellent agreement with both the PHITS and EMPIRE models. Approximately the same trends seen in the comparisons between experiment and simulations with the $^{232}\text{Th}(d, 4n)^{230}\text{Pa}$ reaction channel were observed in this channel. COH, TALYS, and ALICE significantly overestimate the production cross sections, whereas TENDL, PHITS, and EMPIRE underestimate the feeding of this channel.

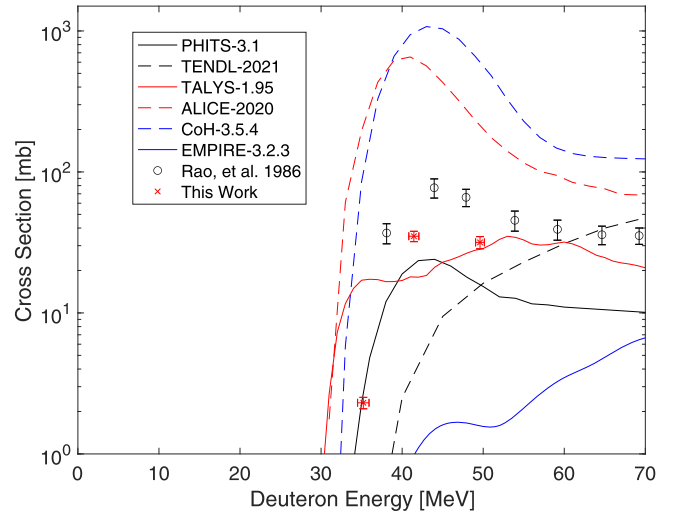


FIG. 9. $^{232}\text{Th}(d, 6n)^{228}\text{Pa}$ independent calculated cross section vs experimental data.

Many of the same arguments made to explain the disagreement between modeling codes and the experimental data for ^{233}Pa apply here as well.

E. $^{232}\text{Th}(d, 6n)^{228}\text{Pa}$ production cross sections

The measured and calculated independent cross sections for the $^{232}\text{Th}(d, 6n)^{228}\text{Pa}$ reaction channel are presented in Fig. 9. Protactinium-228 ($t_{1/2} = 22 \pm 1$ h [34]) decays via electron capture (EC, 98.15%) to ^{228}Th ($t_{1/2} = 1.91 \pm (9.0 \times 10^{-4})$ yr [75]) and α emission (α , 1.85%) to ^{224}Ac ($t_{1/2} = 2.78 \pm 0.17$ h [76]). Since the last foil in this work was near the threshold energy (29.01 MeV) for the $^{232}\text{Th}(d, 6n)^{228}\text{Pa}$ reaction, ^{228}Pa was only detected in three of the four foils. As shown, our cross sections show a maximum of 34.9 ± 3.4 mb at approximately 41.4 MeV. Above 35 MeV, the measured cross sections are within a factor of 2–4 to all predictions from PHITS and TALYS, all of which underpredict this channel. TENDL and EMPIRE fail to predict the compound peak of the channel. COH and ALICE significantly overpredict the cross sections, far more than any of the other (d, xn) channels reported here.

Theoretical data for this reaction were compared to the experimental data from this work as well as the experimental data from Rao *et al.* [68]. The data from Rao *et al.* [68] reported slightly higher cross section values than those reported here. As mentioned before, Rao *et al.* [68] used different γ -ray intensities than are reported now. For ^{228}Pa γ -ray intensity at 911.204 keV, Rao *et al.* used 6%, but the value reported in the Nuclear Data Sheets is $23.0 \pm 1.1\%$, meaning our intensity is higher by $\approx 74\%$ [34].

V. DISCUSSION

In this work, we have reported excitation functions for ^{228}Pa , ^{229}Pa , ^{230}Pa , ^{232}Pa , and ^{233}Pa via deuteron-induced reactions on thin natural Th foils. The measured cross sections for the $^{232}\text{Th}(d, 5n)^{229}\text{Pa}$ reaction channel show a

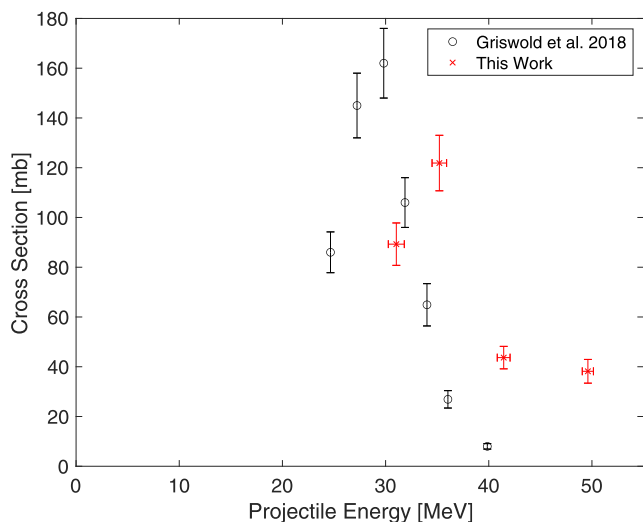


FIG. 10. Measured independent cross sections for $^{232}\text{Th}(d, 5n)^{229}\text{Pa}$ and $^{232}\text{Th}(p, 4n)^{229}\text{Pa}$ [78].

promising possible pathway for ^{229}Th production. Based on the $^{232}\text{Th}(d, 5n)^{229}\text{Pa}$ experimental measurements, shown in Fig. 8, a 1 year irradiation of an incident beam of 50 MeV deuteron with 200 μA on a thick target (1.74 g/cm^2) would yield $\approx 1\text{ mCi}$ of ^{229}Th . The thick target yield was calculated using Radionuclide Yield Calculator software [77]. Figure 10 shows the measured independent cross sections for ^{229}Pa for both pathways using proton and deuteron projectiles [78]. The data from Griswold *et al.* [78] reported a higher peak than for the $^{232}\text{Th}(d, 5n)^{229}\text{Pa}$ channel, but the data from deuteron production may lead to a slightly wider excitation function and, in turn, a higher integral cross section. Further measurements at incident deuteron energies below 31 MeV could confirm this hypothesis.

Many interesting observations may be made in benchmarking the modeling results against the experimental data measured here and previously published data. Because of the small number of channels observed, which are purely limited to (d, xn) channels, broader interpretation is difficult, and a global parametrization is impossible [15,37]. However, we will still attempt to identify common trends observed in the reported reaction channels. In general, TALYS and TENDL seem to do a good job of predicting the shape of most reaction channels, with minor errors in reaction thresholds. Both tend to overestimate the feeding of most channels, but this is not surprising because of the relative lack of experimental reaction data to date. EMPIRE and PHITS modeling show a comparable level of agreement with the experimental data from this work, but they tend to underestimate the observed reaction channels except for the (d, n) and $(d, 2n)$ channels. Additionally, these codes suggest enhanced preequilibrium feeding of many channels, as well as discrete bumps in the excitation function at higher energies, not seen in the experimental data. This behavior suggests that the competition between adjacent (d, xn) and (d, pxn) or $(d, \alpha xn)$ channels is not being correctly calculated by these codes. However, this is purely conjecture, as no Th or Ac reaction products

were observed, and no experimental measurements of any $^{232}\text{Th}(d, pxn)$ or $(d, \alpha xn)$ channels exist. Because of the high Coulomb barrier for nuclei near $Z = 91$ inhibiting proton and α particle emission, these channels are expected to be weakly fed, making it difficult to see $Z < 91$ products or to determine the independent cross sections needed to analyze the reaction dynamics. Without such observations, interpretation of these modeling deficiencies becomes a difficult task.

A more dramatic example of modeling issues is present in the results of both ALICE and COH for nearly every channel. Most notably for (d, n) and $(d, 2n)$ —but seen in the other channels as well—these codes fail to reproduce both the shape and magnitude of all channels observed here, with a magnitude discrepancy of more than a factor of 10 in the $(d, 5n)$ and $(d, 6n)$ channels. The fact that these codes, and these codes alone, so drastically fail to match experimental data leads to a couple of possible explanations. The clear overestimation of all channels indicates that the estimation of the (d, f) channel has been significantly miscalculated by these codes. Miscalculating competition between (d, xn) and (d, pxn) or $(d, \alpha xn)$ channels is expected to be seen in alternating over/underestimation of the (d, xn) channels, as seen in the results of the other codes. However, the consistent overestimation of all (d, xn) channels, combined with the magnitude of this discrepancy, points to a significant underestimation of the fission channel magnitude overall, and the radiochemical separations discussed in Sec. II C. make it clear that fission products were a measurable component of the total reaction yields. This significant underestimation of (d, f) in COH and ALICE is not completely surprising, as fission dynamics are highly sensitive to the angular momentum of the compound nuclear state, and ALICE does not conserve spin or parity in its Weisskopf-Ewing calculations. COH and ALICE are both reliant upon internal models for the calculation of the fission barriers, suggesting a significant overestimation of the effective barrier potentials. For cases where the fission barrier height (B_f) is considerably greater than the neutron binding energy (B_n), i.e., subactinides, almost all of the nonelastic cross section goes into residual product yields (i.e., production cross sections for product nuclei). As a result, a 10%–50% error in the fission channel cross section (if much less than those for residual products) does not change the residual product fits in a calculation. However, if B_f is near the particle binding energy (i.e., for actinide targets), fission yields can dominate; a small error in calculated fission cross sections can have a huge effect on residual product yields: a difference of two large numbers. Additionally, COH results, particularly for statically deformed actinide and lanthanide targets, are highly sensitive to the β_2 deformation parameter required in its input file, taken here as $\beta_2 = 0.205$, from the FRDM2012 tables [79]. Combined with the fact that COH’s Kalbach pickup parametrization is known to significantly overestimate preequilibrium in (d, x) reactions, and that it consistently predicted the strong population of multiple $J > 60$ high-spin states, it is clear that the use of moderate-energy (d, x) reactions presents a particularly savage modeling region for both COH and ALICE. Additional measurements are likely to help improve this state of modeling, particularly if the effects of angular momentum can be

improved in the modeling of actinide targets, as well as a potential reevaluation of the An optical model parametrization for deuterons [58] in this mass region and improved fission barrier tables.

VI. CONCLUSION

Experimentally measured cross sections are reported for several Pa isotopes produced from deuteron-induced reactions on Th targets, and the $^{232}\text{Th}(d, 5n)^{229}\text{Pa}$ reaction cross sections are reported for the first time. The measured experimental cross sections for the other Pa isotopes are consistent with published results from previous measurements. Because of the long half-life of ^{229}Th ($t_{1/2} = 7880 \pm 120$ yr [11]), a long irradiation is needed to achieve a useful quantity of ^{229}Th for generator applications (millicurie levels). Based on the reported cross sections for ^{229}Pa , a one-year dedicated production run with an optimized thick target (1.74 g/cm²) can be estimated to yield approximately 1 mCi of ^{229}Th generator material, which could be milked to yield approximately 7 mCi of ^{225}Ac per year.

Calculated cross sections were compared with the experimental measurements reported in this work and previous literature data, and this benchmarking is the first extension of our recent work to deuteron-induced reactions or actinide targets. Overall, nuclear reaction modeling calculations show passable agreement (within a factor of 2) with measured independent and cumulative cross sections for the product nuclei reported in this work. Generally, PHITS and EMPIRE underestimate experimental cross sections, and TALYS and the TENDL library overestimate, though they all generally predict the correct shape for most channels aside from the strength of preequilibrium particle emission. On the other hand, ALICE and COH both failed to reproduce the shape and magnitude of all experimental cross sections, with significant (factors of 5 to more than 10) disagreement in magnitude, likely due to poor modeling of fission barriers in actinide targets and

the spin-dependence of reaction dynamics in this energy and mass region. Although these modeling codes are useful to predict and optimize accelerator production of radioisotopes for future experiments, the modeling discrepancies shown here clearly illustrate the need to improve the predictive capabilities of deuteron-induced reaction modeling. Such a comparison between calculated cross sections and experimental data can provide insight into possible improvements in the physics models employed by these transport codes. These results serve to further suggest that future measurements and benchmarking of light ion-induced reactions are needed to improve the fidelity of modeling codes for the application community.

The U.S. Department of Energy will provide public access to these results of federally sponsored research in accordance with the DOE Public Access Plan [80].

ACKNOWLEDGMENTS

This research is supported by the U.S. Department of Energy Isotope Program, managed by the Office of Isotope R&D and Production within the DOE Office of Science. ORNL is managed by UT-Battelle, LLC, under Contracts No. DE-AC05-00OR22725 and No. DE-SC0020140 for the U.S. Department of Energy. This work was carried out under the auspices of the U.S. Department of Energy by Lawrence Berkeley National Laboratory and the U.S. Nuclear Data Program under Contract No. DE-AC02-05CH11231. The work of N.B. was supported by the Kuwait Foundation for the Advancement of Sciences (KFAS) under the Research Capacity Building/Scholarship Bridging Program. The publisher, by accepting the article for publication, acknowledges that the U.S. government retains a nonexclusive, paid-up, irrevocable, worldwide license to publish or reproduce the published form of this paper, or allow others to do so, for U.S. government purposes.

-
- [1] M. R. McDevitt *et al.*, *Science* **294**, 1537 (2001).
 - [2] A. M. Ballangrud, W. H. Yang, S. Palm, R. Enmon, P. E. Borchardt, V. A. Pellegrini, M. R. McDevitt, D. A. Scheinberg, and G. Sgouros, *Clin. Cancer Res.* **10**, 4489 (2004).
 - [3] A. Morgenstern, F. Bruchertseifer, and C. Apostolidis, *Curr. Radiopharm.* **5**, 221 (2012).
 - [4] S. Pommé *et al.*, *Appl. Radiat. Isot.* **70**, 2608 (2012).
 - [5] M. S. Basunia, *Nucl. Data Sheets* **181**, 475 (2022).
 - [6] E. Browne, *Nucl. Data Sheets* **93**, 763 (2001).
 - [7] R. Abergel, D. An, A. Lakes, J. Rees, and S. Gauny, *J. Med. Imaging Radiat. Sci.* **50**, S23 (2019).
 - [8] Z. Jiang, E. Revskaya, D. R. Fisher, and E. Dadachova, *Curr. Radiopharm.* **11**, 215 (2018).
 - [9] G. Sgouros, E. Frey, B. He, N. Ray, and D. Ludwig, *J. Med. Imaging Radiat. Sci.* **50**, S110 (2019).
 - [10] G. Sgouros, B. He, N. Ray, D. L. Ludwig, and E. C. Frey, *EJNMMI Phys.* **8**, 60 (2021).
 - [11] E. Browne and J. K. Tuli, *Nucl. Data Sheets* **109**, 2657 (2008).
 - [12] B. Seiferle *et al.*, *Nature (London)* **573**, 243 (2019).
 - [13] M. K. Covo *et al.*, *2017 IEEE International Workshop on Metrology for AeroSpace* (IEEE, Piscataway, NJ, 2017), p. 484.
 - [14] J. T. Morrell, A. S. Voyles, M. S. Basunia, J. C. Batchelder, E. F. Matthews, and L. A. Bernstein, *Eur. Phys. J. A* **56**, 13 (2020).
 - [15] M. B. Fox *et al.*, *Phys. Rev. C* **103**, 034601 (2021).
 - [16] A. S. Voyles, A. M. Lewis, J. T. Morrell, M. S. Basunia, L. A. Bernstein, J. W. Engle, S. A. Graves, and E. F. Matthews, *Eur. Phys. J. A* **57**, 94 (2021).
 - [17] A. Hermanne *et al.*, *Nucl. Data Sheets* **148**, 338 (2018).
 - [18] J. T. Morrell, computer code NPAT: Nuclear physics analysis tools, 2019.
 - [19] A. S. Voyles, L. A. Bernstein, E. R. Birnbaum, J. W. Engle, S. A. Graves, T. Kawano, A. M. Lewis, and F. M. Nortier, *Nucl. Instrum. Methods. Phys. Res. Sect. B* **429**, 53 (2018).
 - [20] S. Takács, F. Tárkányi, B. Király, A. Hermanne, and M. Sonck, *Nucl. Instrum. Methods. Phys. Res. Sect. B* **251**, 56 (2006).
 - [21] M. U. Khandaker, H. Haba, M. Murakami, N. Otuka, and H. A. Kassim, *J. Radiol. Nucl. Chem.* **302**, 759 (2014).

- [22] P. Jung, *J. Nucl. Mater.* **144**, 43 (1987).
- [23] T. Zhenlan, Z. Fuying, and W. Gongqing, Report No. CNIC-00810; CNDC-0013; INDC(CPR)-031/L, <https://www.osti.gov/etdweb/biblio/174199>.
- [24] A. Hermanne, M. Sonck, S. Takács, and F. Tárkányi, *Nucl. Instrum. Methods Phys. Res. Sect. B.* **161**, 178 (2000).
- [25] K. Ochiai, M. Nakao, N. Kubota, S. Sato, M. Yamauchi, N. H. Ishioka, T. Nishitani, and C. Konno, *2007 International Conference on Nuclear Data for Science and Technology* (EDP Sciences, Les Ulis, France, 2007), p. 1011.
- [26] B. Király, S. Takács, F. Ditrói, F. Tárkányi, and A. Hermanne, *Nucl. Instrum. Methods Phys. Res. Sect. B.* **267**, 15 (2009).
- [27] M. U. Khandaker, H. Haba, J. Kanaya, and N. Otuka, *Nucl. Instrum. Methods Phys. Res. Sect. B.* **316**, 33 (2013).
- [28] M. Avrigeanu *et al.*, *Phys. Rev. C* **89**, 044613 (2014).
- [29] J. R. Griswold *et al.*, *Appl. Radiat. Isot.* **118**, 366 (2016).
- [30] V. Radchenko, J. W. Engle, J. J. Wilson, J. R. Maassen, M. F. Nortier, E. R. Birnbaum, K. D. John, and M. E. Fassbender, *Radiochim. Acta* **104**, 291 (2016).
- [31] P. D. Hopkins *et al.*, *Dalton Trans.* **47**, 5189 (2018).
- [32] E. Browne, *Nucl. Data Sheets* **107**, 2579 (2006).
- [33] E. Browne and J. K. Tuli, *Nucl. Data Sheets* **113**, 2113 (2012).
- [34] K. Abusaleem, *Nucl. Data Sheets* **116**, 163 (2014).
- [35] B. Singh, J. K. Tuli, and E. Browne, *Nucl. Data Sheets* **170**, 499 (2020).
- [36] K. Kolos *et al.*, *Phys. Rev. Res.* **4**, 021001 (2022).
- [37] M. B. Fox *et al.*, *Phys. Rev. C* **104**, 064615 (2021).
- [38] T. Sato *et al.*, *J. Nucl. Sci. Technol.* **55**, 684 (2018).
- [39] A. Boudard, J. Cugnon, J. C. David, S. Leray, and D. Mancusi, *Phys. Rev. C* **87**, 014606 (2013).
- [40] L. Silver, A. Kohama, K. Iida, K. Oyamatsu, S. Hashimoto, H. Iwase, and K. Niita, *Nucl. Instrum. Methods Phys. Res. Sect. B.* **334**, 34 (2014).
- [41] N. Burahmah, J. R. Griswold, L. H. Heilbronn, and S. Mirzadeh, *Appl. Radiat. Isot.* **172**, 109676 (2021).
- [42] A. J. Koning, S. Hilaire, and M. C. Duijvestijn, *International Conference on Nuclear Data for Science and Technology, 26 September–1 October 2004, Santa Fe, NM*, AIP Conf. Proc. No. 769 (AIP, New York, 2005), p. 1154.
- [43] A. J. Koning and D. Rochman, *Nucl. Data Sheets* **113**, 2841 (2012).
- [44] A. J. Koning and J. P. Delaroche, *Nucl. Phys. A.* **713**, 231 (2003).
- [45] S. Watanabe, *Nucl. Phys.* **8**, 484 (1958).
- [46] D. G. Madland, Report No. LA-UR-88-376; CONF-880232-4, Los Alamos National Laboratory (LANL), Los Alamos, NM (United States), <https://www.osti.gov/biblio/5260574>.
- [47] A. Gilbert and A. G. W. Cameron, *Can. J. Phys.* **43**, 1446 (1965).
- [48] A. J. Koning, D. Rochman, J. C. Sublet, N. Dzysiuk, M. Fleming, and S. van der Marck, *Nucl. Data Sheets* **155**, 1 (2019).
- [49] A. Koning, computer code ISOTOPIA-1.0, 2019.
- [50] M. Blann and H. K. Vonach, *Phys. Rev. C* **28**, 1475 (1983).
- [51] M. Blann, *Phys. Rev. C* **54**, 1341 (1996).
- [52] A. Nadasen, P. Schwandt, P. P. Singh, W. W. Jacobs, A. D. Bacher, P. T. Debevec, M. D. Kaitchuck, and J. T. Meek, *Phys. Rev. C* **23**, 1023 (1981).
- [53] T. D. Thomas, *Phys. Rev.* **116**, 703 (1959).
- [54] B. L. Berman and S. C. Fultz, *Rev. Mod. Phys.* **47**, 713 (1975).
- [55] S. K. Kataria, V. S. Ramamurthy, and S. S. Kapoor, *Phys. Rev. C* **18**, 549 (1978).
- [56] S. K. Kataria, V. S. Ramamurthy, M. Blann, and T. T. Komoto, *Nucl. Instrum. Methods Phys. Res. Sect. A* **288**, 585 (1990).
- [57] M. Herman, R. Capote, B. V. Carlson, P. Obložinský, M. Sin, A. Trkov, H. Wienke, and V. Zerkin, *Nucl. Data Sheets* **108**, 2655 (2007).
- [58] H. An and C. Cai, *Phys. Rev. C* **73**, 054605 (2006).
- [59] M. Avrigeanu, A. C. Obreja, F. L. Roman, V. Avrigeanu, and W. Von Oertzen, *At. Data Nucl. Data Tables* **95**, 501 (2009).
- [60] T. Belgya *et al.*, *Handbook for Calculations of Nuclear Reaction Data, RIPL-2, IAEA-TECDOC-1506* (IAEA, Vienna, 2006).
- [61] A. D'Arrigo, G. Giardina, M. Herman, A. V. Ignatyuk, and A. Taccone, *J. Phys. G: Nucl. Part. Phys.* **20**, 365 (1994).
- [62] T. Kawano, P. Talou, M. B. Chadwick, and T. Watanabe, *J. Nucl. Sci. Technol.* **47**, 462 (2010).
- [63] P. Talou, T. Kawano, and I. Stetcu, *Phys. Pro* **47**, 39 (2013).
- [64] T. Kawano, Report No. JAEA-CONF-2019-001, https://inis.iaea.org/search/search.aspx?orig_q=RN:51045860.
- [65] T. Kawano, in *Compound-Nuclear Reactions*, edited by J. Escher *et al.* (Springer, Cham, 2021), p. 27.
- [66] V. Avrigeanu, P. E. Hodgson, and M. Avrigeanu, *Phys. Rev. C* **49**, 2136 (1994).
- [67] C. Duchemin, A. Guertin, F. Haddad, N. Michel, and V. Metivier, *Phys. Med. Biol.* **60**, 931 (2015).
- [68] J. R. Rao, J. Ernst, and H. Machner, *Nucl. Phys., Sect. A* **448**, 365 (1986).
- [69] L. Northcliffe and R. Schilling, *At. Data Nucl. Data Tables* **7**, 233 (1970).
- [70] Y. A. Akovali, *Nucl. Data Sheets* **77**, 433 (1996).
- [71] S. Singh, A. K. Jain, and J. K. Tuli, *Nucl. Data Sheets* **112**, 2851 (2011).
- [72] T. Mastren *et al.*, *Anal. Chem.* **90**, 7012 (2018).
- [73] T. Mastren, A. Akin, R. Copping, M. Brugh, D. S. Wilbur, E. R. Birnbaum, F. M. Nortier, K. D. John, and M. E. Fassbender, *Nucl. Med. Biol.* **90-91**, 69 (2020).
- [74] M. T. Friend, T. Mastren, T. G. Parker, C. E. Vermeulen, M. Brugh, E. R. Birnbaum, F. M. Nortier, and M. E. Fassbender, *Appl. Radiat. Isot.* **156**, 108973 (2020).
- [75] S. Singh and B. Singh, *Nucl. Data Sheets* **130**, 127 (2015).
- [76] E. Browne and J. K. Tuli, *Nucl. Data Sheets* **112**, 1115 (2011).
- [77] M. Sitarz, E. Nigrón, A. Guertin, F. Haddad, and T. Matulewicz, *Instruments* **3**, 7 (2019).
- [78] J. R. Griswold, C. U. Jost, D. W. Stracener, S. H. Bruffey, D. L. Denton, M. A. Garland, L. Heilbronn, and S. Mirzadeh, *Phys. Rev. C* **98**, 044607 (2018).
- [79] P. Möller, A. J. Sierk, T. Ichikawa, and H. Sagawa, *At. Data Nucl. Data Tables* **109-110**, 1 (2016).
- [80] <http://energy.gov/downloads/doe-public-access-plan>.

Correction: The surname of the seventh author contained a spelling error and has been fixed.